RIS for Signal Cancellation in 3D

Xue Wei*, Anushka Gupta*, Aveek Dutta*, Dola Saha* and Gregory Hellbourg†
*Department of Electrical and Computer Engineering, University at Albany, SUNY
†Department of Astronomy, California Institute of Technology
Email: *{xwei4, agupta, adutta, dsaha}@albany.edu, †ghellbourg@astro.caltech.edu

***Abstract*—We present a novel application of Reconfigurable Intelligent Surfaces (RIS) for signal cancellation, with particular focus on eliminating radio frequency interference (RFI) cancellation in Radio Astronomy Services (RAS). While existing RIS applications focus on directing reflected electromagnetic (EM) waves to either enhance or null the wave-front, our work cancels RFI by adaptive redirection of EM waves in a three-dimensional space. RAS plays a crucial role in the exploration and understanding of the universe by detecting and analyzing radio emissions from celestial bodies. However, RFI emanating from human-made sources weakens the faint astronomical signals and affect astronomical observations. To address this challenge, we outline 3D RFI cancellation system by a novel RIS design to jointly control the phase and amplitude in specific Directions of Reflection (DoR) to comprehensively cancel any incident RFI on the telescope. We provide a blueprint, supported by analysis, for prototyping such an RIS array and evaluate its performance in a practical setting for multiple Direction of Arrival (DoA). Our results indicate that the RFI from Automatic Dependent Surveillance–Broadcast (ADS-B) from aircrafts can be fully canceled with a relative cancellation error of 1.0181×10^{-4}.**

***Keywords*—Reconfigurable intelligent surfaces, Radio frequency interference cancellation, Radio astronomy services.**

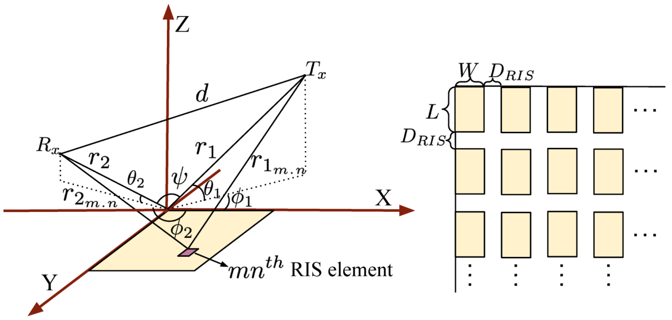

Fig. 1: 3D geometric view of the RFI cancellation system: The airborne RFI source, T_x, with Az-El: $[\phi_1, \theta_1]$, is at an unknown distance, r_1 from the origin $0, 0, 0$, the top-left corner of the RIS located on the ground (X-Y) plane. The telescope receiver, R_x is located at a known distance, r_2 from the origin with a known Az-El: $[\phi_2, \theta_2]$. Given this 3D geometry, the goal is to design an $M \times N$ RIS array with prior knowledge of the DoA [2] and the DoR (fixed) relative to the RIS array.

I. INTRODUCTION

Reconfigurable Intelligent Surfaces (RIS) has emerged as a transformative technology, designed as an array of passive metamaterial patches or antennas, that reflect incoming electromagnetic (EM) waves in an adaptive manner [1]. This is achieved by intelligently adjusting the *phase and amplitude of reflected waves*, which in turn enables control over the signal propagation environment. Strategically placing these surfaces within communication environment allows RIS to achieve a variety of objectives, such as, enhancing signal strength in a particular direction, interference avoidance by beam-nulling or optimizing the overall coverage of wireless networks. Although RIS has many compelling use cases, its application in the area of *interference and/or signal cancellation* is missing from the literature, whether it is for controlled cancellation of harmful interference at a wireless receiver or targeted adversarial attacks in a contested wireless environment. In this work, we specifically focus on a principled approach towards designing RIS array for precise cancellation of signals from air-borne transmitters at radio telescope receivers with relative positions in a 3-dimensional space.

There is a rich literature on employing RIS to direct the reflected EM waves in a specific direction, typically with the goal to either enhance or null the wave-front. In contrast, we prioritize successful cancellation of Radio Frequency Interference (RFI) at the telescope receiver (a specific coordinate in a 3D space) by redirecting EM waves in any direction as needed. This is starkly different from the widely used generalized Snell's law [3], which primarily ensures the direction of the reflected beam towards the desired direction without considering the phase and energy of the reflected beam. *However, in signal cancellation, a careful calculation and simultaneous control of the phase and amplitude of the reflected signal in a given Direction-of-Reflection (DoR) is critical to guarantee complete cancellation of the incident RFI.*

Cancelling RFI in Radio Telescopes: As the radio spectrum becomes increasingly congested due to proliferation of *new* wireless technologies, unwanted interference from these sources is seen a significant challenge in the field of Radio Astronomy Services (RAS) [4]. RFI can easily overwhelm the faint astronomical signals and weak radio emissions used for astronomical measurements, which makes interference cancellation imperative for preserving the high sensitivity of these instruments. While spatial filtering has been a useful approach for canceling RFI, it carries the risk of inadvertently filtering out astronomical signals itself and reducing the sensitivity of the telescope. Furthermore, RFI from mobile transmitters in space and the air can exhibit varying incident angles and characteristics and involves estimating the direction-of-arrival (DoA) of the RFI, which complicates the task of cancellation. In order to focus on the design aspects of the RIS for this novel application, we lean on two seminal works that provide key insights to extrapolate the principles of an RFI cancellation system to 3-dimensions [2], [5]. While, prototyping the RIS array for this application is not in the scope of this paper, we present a comprehensive design process along with analysis of a practical equivalent circuit, detailed component modeling and determination of critical dimensions of the RIS array. We support our design with practical simulations using the ADS-B [6] signal as the RFI source and key telescope parameters from the Owens Valley Radio Observatory [7]. For clarity, we organize the paper into *three complementary steps*, each focusing on a specific aspect of the cancellation apparatus. Therefore, the contributions are as follows:

1) We design a novel 3D RFI cancellation system with RIS focusing on precise joint control of *phase and amplitude* of the reflected wave to minimize the residual RFI at the radio telescope: Step-1, §II.
2) We present a geometric analysis of the propagation environment, which lends itself to an equivalent circuit model of the RIS elements: Step-2, §III.
3) We provide a blueprint for prototyping the RIS array through dimensional information, component selection and circuit considerations: Step-3, §IV.
4) We present a simulation analysis of single and multiple DoA scenarios as well as bounds for residual RFI showing the generality of the proposed design and compare RFI cancellation performance using a Uniform Rectangular Array (URA): §V.

II. STEP-1: OPTIMAL REFLECTION COEFFICIENT

A. Estimating the Distance to the Source

Figure 1 illustrates the *Three* main components of the RFI cancellation system: The Telescope receiver (R_x), the airborne source (T_x) and the RIS on the ground (X-Y) plane. The top-left corner of the RIS is considered as the origin, $(0, 0, 0)$ of this 3D coordinate system. All distances and Az-El are calculated with respect to this origin. The DoA of the incident RFI, denoted as (ϕ_1, θ_1) can be accurately estimated in very low SNR by employing algorithms in [2] and is considered to be known for this work. The distance to R_x, r_2 and the DoR, (ϕ_2, θ_2) are also known since the telescope and the RIS are considered to be fixed installations. Therefore, based on this geometry the distance, d of the direct path between the T_x and the R_x and the angle ψ is calculated by using the dot product of the distance vectors $\vec{r_1}$ and $\vec{r_2}$ in (1).

$$d = r_1^2 + r_2^2 - r_1 r_2 \cos\psi \quad \text{and} \quad \cos\psi = \frac{\vec{r_1}\cdot\vec{r_2}}{|\vec{r_1}|\cdot|\vec{r_2}|} \tag{1}$$

Here, r_1 is the distance of the T_x from the origin $(0, 0, 0)$, and ψ represents the angle between the lines r_1 and r_2, as shown in Figure 1. The Cartesian form of the T_x location is obtained from the spherical coordinates, (r_1, ϕ_1, θ_2) as,

$$\vec{r_1} = (r_1\cos\theta_1\cos\phi_1, r_1\cos\theta_1\sin\phi_1, r_1\sin\theta_1) \tag{2}$$

Similarly, $\vec{r_2}$ denotes the distance vector to the telescope, represented in Cartesian coordinates as

$$\vec{r_2} = (r_2\cos\theta_2\cos\phi_2, r_2\cos\theta_2\sin\phi_2, r_2\sin\theta_2) \tag{3}$$

Therefore, from (2) and (3),

$$\vec{r_1}\cdot\vec{r_2} = r_1 r_2\cos\theta_1\cos\theta_2\cos\phi_1\cos\phi_2 + r_1 r_2\cos\theta_1\cos\theta_2\sin\phi_1\sin\phi_2 + r_1 r_2\sin\theta_1\sin\theta_2 \tag{4}$$

Substituting (4) in (1) we calculate $\cos\psi$ as,

$$\cos\psi = \cos\theta_1\cos\theta_2\cos\phi_1\cos\phi_2 + \cos\theta_1\cos\theta_2\sin\phi_1\sin\phi_2 + \sin\theta_1\sin\theta_2 \tag{5}$$

Let's denote the the power and gain of T_x by P_T and G_T respectively. Also, denote the power of the incident RFI at R_x by P_R and that at the RIS array with $M\times N$ elements as P_{RIS}. Therefore, using the Friis transmission equation and substituting d from (1) we get,

$$\frac{P_R}{P_{RIS}} = \frac{P_T\frac{G_T G_R\lambda^2}{(4\pi d)^2}}{P_T\frac{M^2N^2G_T G_r\lambda^2}{(4\pi r_1)^2}} = \frac{G_R r_1^2}{M^2N^2G_r d^2} = \frac{G_R r_1^2}{M^2N^2G_r(r_1^2 + r_2^2 - r_1 r_2\cos\psi)} \tag{6}$$

where, G_r is the gain of each RIS element, G_R represents the directional gain of telescope in the direction of T_x and λ is the wavelength. Since, $r_1 \gg r_2 > 0$ and all other variables in (6) are either known or measurable, the solution for r_1 is,

$$\boxed{r_1 = \frac{r_2 MN}{2|P_R M^2N^2G_r - P_{RIS}G_R|}\left\{\sqrt{P_R^2M^2N^2G_r^2(\cos^2\psi - 4) + 4P_{RIS}G_R P_R G_r} - \operatorname{sgn}(P_R M^2N^2G_r - P_{RIS}G_R)P_R MNG_r|\cos\psi|\right\}} \tag{7}$$

Therefore, (7) allows us to calculate the coordinates of T_x and R_x using (2) and (3) respectively. Also, from figure 1 we find that W and L denote the width and length of each RIS element and D_{RIS} is the spacing between two adjacent elements. Therefore, the location of the mn^{th} element on the X-Y plane in Cartesian coordinates is given by,

$$\vec{R}_{mn} = ((n-0.5)\,W + (n-1)D_{RIS}, (m-0.5)\,L + (m-1)D_{RIS}, 0) \tag{8}$$

Using (2), (3) and (8), the distance between the T_x and the mn^{th} RIS element, denoted by $r_{1_{m.n}}$ and the distance between the R_x and the mn^{th} RIS element, $r_{2_{m.n}}$ is calculated as,

$$r_{1_{m.n}} = \sqrt{\sum_{i=1}^{3}(r_{1_i} - R_{mn_i})^2};\, r_{2_{m.n}} = \sqrt{\sum_{i=1}^{3}(r_{2_i} - R_{mn_i})^2} \tag{9}$$

The distance in (9) is used to calculate the phase and amplitude for each RIS element that it will have to be programmed to, for canceling the RFI at the telescope receiver.

B. Amplitude and Phase Solution

The power of the RFI at R_x and that captured by the mn^{th} RIS element from T_x is given by Friis transmission formula,

$$P_R = P_T\frac{G_T G_R\lambda^2}{(4\pi d)^2} \quad ; \quad P^i_{m,n} = P_T\frac{G_T G_r\lambda^2}{(4\pi r_{1_{m,n}})^2} \tag{10}$$

Similarly, the power of the reflected signal received by the R_x from the mn^{th} RIS element is,

$$P_{R_{m,n}} = P^i_{m,n}\frac{G'_R G_r \lambda^2}{(4\pi r_{2_{m,n}})^2} = \frac{P_T G_T G_r^2 G'_R \lambda^4}{(4\pi r_{1_{m,n}})^2(4\pi r_{2_{m,n}})^2} \quad (11)$$

where G'_R is the directive gain (or the side-lobe gain) of the telescope in the direction of the RIS array.

Now, in order to cancel the incident RFI at R_x, the reflected wave from the RIS must exert precisely the inverse influence of the direct path from the T_x. Let a_d and ϕ_d denote the channel gain and phase-shift associated with the direct path of the RFI, while $a_{m,n}$ and $\phi_{m,n}$ are the channel gain and phase-shift of the reflected path by the mn^{th} RIS element. Therefore, for complete cancellation the sum of the reflected RFI from each element and the direct RFI must equal zero, expressed as,

$$\boxed{\left| a_d e^{j\phi_d} + \sum_{m=1}^{M}\sum_{n=1}^{N} a_{m,n}\Gamma_{m,n}e^{j\phi_{\Gamma_{m,n}}} \right| = 0} \quad (12)$$

where, $\Gamma_{m,n}$ is the reflection coefficient for the mn^{th} element and characterizes the extent to which a wave is reflected due to an impedance discontinuity within the transmission medium [8]. In general, $\Gamma_{m,n} = |\Gamma_{m,n}|e^{j\phi_{\Gamma_{m,n}}}$ is a complex quantity where $|\Gamma_{m,n}|$ controls the energy of the reflected wave from the mn^{th} RIS element. This is strategically designed to match the energy of the direct RFI signal received at the telescope. Meanwhile, $\phi_{\Gamma_{m,n}}$ denotes the phase delay assigned to the mn^{th} RIS element to achieve an opposite phase compared to the direct RFI signal received in the telescope.

1) Amplitude Solution of $\Gamma_{m,n}$*:* From (12), we observe that in order to achieve the *amplitude equality* requirement for cancellation, the RIS elements need to satisfy the following,

$$\sum_{m=1}^{M}\sum_{n=1}^{N} a_{m,n}|\Gamma_{m,n}| = a_d \quad (13)$$

In other words, the sum of the magnitude of all individual reflected waves from each element is equal to a_d. Since, $a_d{=}\sqrt{P_R}$ and $a_{m,n}{=}\sqrt{P_{R_{m.n}}}$, we substitute (10) and (11) in (13) and simplify to obtain the expression of $\Gamma_{m,n}$,

$$\sum_{m=1}^{M}\sum_{n=1}^{N} \frac{|\Gamma_{m,n}|}{r_{1_{m,n}} r_{2_{m,n}}} = \frac{4\pi}{dG_r\lambda}\sqrt{\frac{G_R}{G'_R}} \quad (14)$$

Since the size (W, L) of the elements and their spacing (D_{RIS}) is significantly small compared to the distances, r_1 and r_2, the variation in the reflected energy from different RIS elements is negligible. Consequently, we can disregard the distinctions between $r_{1_{m.n}}$ and $r_{2_{m.n}}$ and substitute $r_{1_{m.n}}{=}r_1$ and $r_{2_{m.n}}{=}r_2$ for simplification. Therefore, the magnitude of the reflection coefficient for each element is,

$$\sum_{m=1}^{M}\sum_{n=1}^{N} |\Gamma_{m,n}| = \frac{4\pi r_1 r_2}{dG_r\lambda}\sqrt{\frac{G_R}{G'_R}} \quad (15)$$

Assuming, that the magnitude of the reflection coefficient for all elements is the same, we can write,

$$\boxed{|\Gamma_{m,n}| = \frac{4\pi r_1 r_2}{MNdG_r\lambda}\sqrt{\frac{G_R}{G'_R}}} \quad (16)$$

2) Phase Solution of $\Gamma_{m,n}$*:* Similar to the amplitude solution, the *phase inversion* requirement for cancellation is fulfilled by assigning the phase for each element as,

$$\phi_{m,n} + \phi_{\Gamma_{m,n}} = \phi_d + \pi \quad (17)$$

This ensures that the reflected wave from each RIS element has the *exact opposite phase* compared to that of the direct path. The phase-shift, $\phi_{m,n}$ is solely due to the path delays of the reflected wave that depends on the relative positions of the T_x, R_x and the RIS as shown in figure 1. Therefore, based on the geometry we express the phase-shift as,

$$\phi_{m,n} = 2\pi\frac{r_{1_{m,n}} + r_{2_{m,n}}}{\lambda} \quad (18)$$

Substituting (18) in (17), the phase-shift for each element is,

$$\boxed{\phi_{\Gamma_{m,n}} = \pi + 2\pi\frac{d - r_{1_{m,n}} - r_{2_{m,n}}}{\lambda}} \quad (19)$$

Therefore, the goal of the remainder of the paper is to derive the specifications of a suitable RIS array that implements the amplitude and phase solution in (16) and (19) such that the resulting Γ_{mn} satisfies the cancellation described by (12) over a wide range of DoA for given DoR.

III. STEP-2: RIS EQUIVALENT CIRCUIT

A. Dimensional Design

The RIS array is envisioned to be implemented on Printed Circuit Board (PCB) technology with utilizing two metal layers at the top and bottom with a dielectric material (or substrate) in between. The substrate maintains the necessary spacing and provides mechanical support between the components in the top layer and its ground plane. The RIS elements are a combination of metallic patch, PIN diodes and varactor diodes along with bias and ground lines as required. The combined effect of the PIN and varactor diodes provides the flexibility for precise simultaneous control over the amplitude and the angle of the reflection coefficient for each element. $\Gamma_{m,n}$, which is not required in other RIS applications.

The metal patches on the substrate essentially function as microstrip patch antennas, whose dimensions depend on some key specifications [12]–[14]. The patch length L is given by,

$$L = c/2f_c\sqrt{(\epsilon_r + 1)/2} \quad (20)$$

where, c is the speed of light, ϵ_r is the dielectric constant of the substrate and f_c is the operating frequency. The patch width (W) is given by,

$$W{=}\frac{c}{2f_c\sqrt{\epsilon_{eff}}}{-}0.824H\left[\frac{(\epsilon_{eff}{+}0.3)\left(\frac{L}{H}{+}0.264\right)}{(\epsilon_{eff}{-}0.258)\left(\frac{L}{H}{+}0.8\right)}\right] \quad (21)$$

where H is the thickness of the substrate and ϵ_{eff} is the effective dielectric constant given by,

$$\epsilon_{eff} = \frac{\epsilon_r + 1}{2} + \frac{\epsilon_r - 1}{2}\left[\frac{1}{\sqrt{1 + 12\left(\frac{H}{L}\right)}}\right] \quad (22)$$

B. Equivalent Circuit Model

A large majority of RIS designs in the literature employ either a single PIN diode or a single varactor diode for each

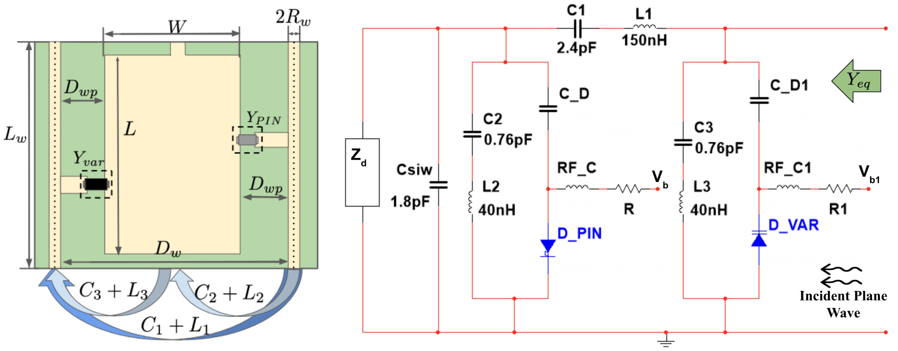

(a) Top view of an element

(b) Equivalent circuit of an element

Parameter	**Value**	**Reference**
W, L	(81.9, 69.1) mm	(20), (21), (22)
D_{wp}	13.1 mm	§IV-A
D_w, L_w, R_w	(87.8, 83, 1) mm	§IV-A
C_1, L_1	2.4 pF, 150 nH	(25)
C_2, C_3	0.764 pf	(26a)
L_2, L_3	40.42 nH	(26b)
C_{SIW}	1.8 pF	[9]
Z_d	j1.0515 Ω	(24)
Y_{eq}	*Variable*	(30), (31), (32)
f_c, λ	1090 Mhz, 275 mm	ADS-B [6]
D_{var}	SMV1405	Skyworks [10]
D_{PIN}	UM4000/UM4900	Microsemi [11]

(c) RIS parameter table

Fig. 2: A dimensional drawing and equivalent circuit model of one element of the proposed RIS array. The parameter table shows the different values of the circuit components along with references to the calculation of the corresponding values.

element. The goal is to vary the impedance of the elements by applying different bias voltages to implement different reflection coefficients. However, our 3D RFI cancellation system necessitates the simultaneous consideration of both amplitude and phase of $\Gamma_{m,n}$. Therefore, our RIS element has both a varactor diode and a PIN diode to achieve simultaneous control of magnitude and phase in the system. Figure 2a shows a dimensional drawing of an element with relative positioning of the components and the corresponding bias lines. We acknowledge that an actual PCB layout may change some of the dimensions but this design provides a strong benchmark for the RFI cancellation apparatus.

Figure 2b shows the equivalent circuit model for the element, where the varactor diode and the PIN diode are biased independently. This configuration provides greater flexibility in adjusting the input impedance, allowing more freedom to adjust the reflection coefficient. The varactor diode functions as a variable capacitor when operated in reverse bias and is modeled as a parallel combination of a resistor (R_{var}) and a variable capacitor (C_{var}), followed by an inductor (L_{var}) in series. In contrast, a PIN diode operates as a current-controlled device in forward bias and is typically used for attenuating, leveling, and modulating RF signals. Additionally, when the control current is switched on and off, it serves as a switch or phase shifter for RF signals. In our specific application, we model the PIN diode is operated in forward bias and functions as a variable resistor. This equivalent circuit of a PIN diode comprises a series connection of an inductor (L_{PIN}) and a variable resistor (R_{PIN}), whose value is inversely proportional to the bias current flowing through the diode. Therefore the admittance of these two devices are given by,

$$Y_{\text{var}}=\frac{\left(j\omega C_{\text{var}}+\frac{1}{R_{\text{var}}}\right)\frac{1}{j\omega L_{\text{var}}}}{j\omega C_{\text{var}}+\frac{1}{R_{\text{var}}}+\frac{1}{j\omega L_{\text{var}}}}\quad ; \quad Y_{\text{PIN}}=\frac{1}{R_{\text{PIN}}+j\omega L_{\text{PIN}}} \tag{23}$$

Furthermore, The dielectric substrate, grounded and modeled as a transmission line with a terminal short-circuit that exhibits an equivalent impedance given by [15],

$$Z_d = j\frac{\eta_0}{\sqrt{\epsilon_r}}\tan\frac{2\pi f_c\sqrt{\epsilon_r}H}{c} \tag{24}$$

where, η_0=377Ω is the characteristic impedance of free space.

Considering the interaction between the transmission (bias) lines and the combination of transmission (bias) lines and metallic patches, three sets of capacitance and inductance are established for each element. These are modeled as impedance per unit length by employing fundamental principles of the transmission line theory [15], [16]. Assuming the bias lines have identical widths, the capacitance and inductance formed between these two bias lines are,

$$C_1=\frac{\pi\epsilon L_w}{\cosh^{-1}(\frac{D_w}{2R_w})}\quad ; \quad L_1=\frac{\mu}{\pi}\cosh^{-1}\left(\frac{D_w}{2R_w}\right)L_w \tag{25}$$

where ϵ=$\epsilon_r\epsilon_0$ is permittivity, where ϵ_0=8.85×10^{-12} Fm^{-1} is the permittivity of air. L_w=L_{w1}=L_{w2} denotes the length of these two transmission lines and R_w=R_{w1}=R_{w2} represents half of the width of these two transmission lines and D_w represents the distance between the center of two lines. $\mu=\mu_0$ is the permeability of vacuum, $4\pi\times 10^{-7}Hm^{-1}$.

When considering the capacitance C_2, C_3 and inductance L_2, L_3 between the transmission line and the metal patch, they can be treated as two lines with different widths. The coplanar inductance and capacitance [16] is given by,

$$C_2=\begin{cases}\frac{\epsilon_r'\ln\left(2\frac{1+\sqrt{k'}}{1-\sqrt{k'}}\right)}{377\pi c}L & ,0\leq k\leq\frac{1}{\sqrt{2}}\\ \frac{\epsilon_r'}{120c\ln\left(2\frac{1+\sqrt{k}}{1-\sqrt{k}}\right)}L & ,\frac{1}{\sqrt{2}}\leq k\leq 1\end{cases} \tag{26a}$$

$$L_2=\begin{cases}\frac{377\pi}{c\ln\left(2\frac{1+\sqrt{k'}}{1-\sqrt{k'}}\right)}L & ,0\leq k\leq\frac{1}{\sqrt{2}}\\ \frac{120}{c}\ln\left(2\frac{1+\sqrt{k}}{1-\sqrt{k}}\right)L & ,\frac{1}{\sqrt{2}}\leq k\leq 1\end{cases} \tag{26b}$$

where, $k=\frac{D_{wp}}{D_{wp}+(W+2R_w)}$, $k'=\sqrt{1-k^2}$ and D_{wp} is the distance between the transmission line and the metal patch. The effective relative permittivity ϵ_r' is given by,

$$\epsilon_r'=\frac{\epsilon_r+1}{2}\Bigg\{\tanh\left[0.775\ln\left(\frac{2H}{W+2R_w}\right)+1.75\right] + \frac{k(W+2R_w)}{2H}[0.04-0.7k+0.01(1-0.1\epsilon_r)(0.25+k)]\Bigg\} \tag{27}$$

C_3 and L_3 are the same as C_2 and L_2. Also, a capacitance, C_{SIW} is formed by metallic vias between adjacent elements.

IV. STEP-3: CIRCUIT MODEL TO PHYSICAL DESIGN

A. Parameter Selection

Based on the geometry based analysis and equivalent circuit model, we provide blueprint for prototyping the RIS array by carefully selecting the components with the optimum set of parameters. For most RIS applications, a H=7 mm thick FR-4 substrate is common with ϵ=4.645 that isolates the top and bottom metal layers. To determine the dimensions of the elements, we use the ADS-B frequency, f_c=1090 MHz [6]. Substituting in (20) and (21) yields, L=61.1 mm and W=81.9 mm. D_{RIS} is chosen to be $\lambda/10$ to limit coupling effects. Other dimensional parameters, summarized in Figure 2 are L_w=83 mm, chosen to be slightly larger than L, R_w=1 mm, to have very similar values for L_1, L_2, and L_3. D_{wp}=13.1 mm, is chosen to accommodate large dimensions of diodes up to several millimeters. Substituting these dimensions and the dielectric constant in (25), (26a) and (26b), we obtain the capacitance and inductance values for the components on the top layer: C_1=2.4 pF, L_1=150 nH, C_2=C_3=0.764 pF, L_2=L_3=40.42 nH and C_{SIW} is 1.8 pF [9].

B. Equivalent Admittance of RIS Element

The reflection coefficient in (16) and (19) for a given DoA is achieved by controlling the equivalent admittance of each RIS element, Y_{eq}, which are related by,

$$\Gamma = \frac{1/\eta_0 - Y_{eq}}{1/\eta_0 + Y_{eq}} \tag{28}$$

Therefore, For brevity, we drop the the element index, m, n since the discussion is focused on one element hereafter.

The equivalent admittance of each element is obtained from the circuit in Figure 2a and (23) as,

$$Y_{eq}=\left[\frac{\left(\frac{1}{Z_a}+\frac{1}{j\omega L_2+\frac{1}{j\omega C_2}}+j\omega C_{\text{SIW}}+Y_{\text{PIN}}\right)\frac{1}{j\omega L_1+\frac{1}{j\omega C_1}}}{\frac{1}{Z_a}+\frac{1}{j\omega L_2+\frac{1}{j\omega C_2}}+j\omega C_{\text{SIW}}+Y_{\text{PIN}}+\frac{1}{j\omega L_1+\frac{1}{j\omega C_1}}}\right] + \frac{1}{j\omega L_3+\frac{1}{j\omega C_3}}+Y_{\text{var}} \tag{29}$$

From (29), it is clear that Y_{eq} strictly depends on fine control of the forward bias level of the PIN diode and reverse bias level for the varactor diode. Substituting the values from the parameter table in Figure 2 and §IV-A in (29) we get,

$$\boxed{Y_{eq}=\frac{-9.9\times10^{-4}-j0.001Y_{\text{PIN}}}{-j0.9514+Y_{\text{PIN}}}-j0.0117+Y_{\text{var}}} \tag{30}$$

Evidently, Y_{var} and Y_{PIN} are the two unknown variables that strictly depend on specific part numbers. For the purposes of canceling RFI in 3-dimensions, the choice of the part will depend on the desired range of values of the capacitance and resistance that can be achieved by that specific device. In order to converge on a specific part we split the complex admittance, into real and imaginary parts. The imaginary part of Y_{PIN} depends on the inductor of the PIN diode model in (23) and remains constant for any forward bias current. Similarly, the real part of Y_{var} solely depends on the resistance in the varactor diode model in (23) and remains constant under reverse bias. Therefore, it is reasonable to set both $\Im(Y_{\text{PIN}})$ and $\Re(Y_{\text{var}})$ to be fixed to determine the required range of PIN diode resistance and varactor diode capacitance.

Therefore, substituting Y_{PIN}=$\Re(Y_{\text{PIN}})+j\Im(Y_{\text{PIN}})$ and Y_{var}=$\Re(Y_{\text{var}})+j\Re(Y_{\text{var}})$ in (30) and separating the real and imaginary parts we get,

$$\Re(Y_{eq}) = \frac{[A+BC]\Re(Y_{\text{PIN}})}{\Re(Y_{\text{PIN}})^2+[\Im(Y_{\text{PIN}})+C]^2}+\Re(Y_{\text{var}}) \tag{31}$$

$$\Im(Y_{eq})=\left[\frac{B[\Re(Y_{\text{PIN}})^2+\Im(Y_{\text{PIN}})^2]+[BC-A]\Im(Y_{\text{PIN}})-AC}{\Re(Y_{\text{PIN}})^2+[\Im(Y_{\text{PIN}})+C]^2}\right] +D+\Im(Y_{\text{var}}) \tag{32}$$

where, the constants A, B, C, D are:

$$A=\left(\frac{1}{Z_a}+\frac{1}{j\omega L_2+\frac{1}{j\omega C_2}}+j\omega C_{SIW}\right)\frac{1}{j\omega L_1+\frac{1}{j\omega C_1}}=-9.9\times10^{-4}$$

$$B=\frac{1}{\frac{1}{\omega C_1}-\omega L_1}=-0.001$$

$$C=\frac{1}{jZ_a}+\frac{1}{\frac{1}{\omega C_2}-\omega L_2}+\omega C_{SIW}+\frac{1}{\frac{1}{\omega C_1}-\omega L_1}=-0.9514$$

$$D=\frac{1}{\frac{1}{\omega C_3}-\omega L_3}=-0.0117$$

Substituting the values of the components in the expression for A, B, C, D we obtain the simplified expressions for the real and imaginary parts of the equivalent admittance for each RIS element, which leads to selecting the specific parts.

C. Component Selection and Quantization

We designate $\Im(Y_{\text{PIN}})$=$-C$ and $\Re(Y_{\text{var}})$=2×10^{-5} that yield $R_{\text{pin}}\in\{500{:}1000\Omega\}$ and $C_{\text{var}}\in\{1{:}2.5\text{pF}\}$. These range of values can be achieved by Microsemi UM4000/UM4900 PIN diode, and the Skyworks SMV1405 varactor diode. In order to limit the number of control bits used to change the forward and reverse biases, we propose a 4-bit quantization that will provide 16 independent and unique bias levels for the two diodes. Consequently, the achieved reflection coefficient by the RIS elements, Γ_A obtained from (28) will differ from the the desired or target reflection coefficient, Γ_T obtained from (16) and (19). This leads to a residual RFI at the telescope and can be seen as a way to balance between hardware complexity and accuracy. In the following section, we show the performance of the proposed RIS design with the chosen components for different DoA and study the residual RFI.

V. EVALUATION AND RESULTS

A. Simulation setup

We simulate the RFI environment as shown in Figure 1 in MATLAB. The distance between the telescope and the origin, r_2=17 m and the ratio G_R/G'_R=1 considering that the direct RFI and reflected RFI are both captured by the same side-lobe of the telescope when the transmitter is at a far away distance from the telescope, r_1=13054 m calculated using (7) and assuming the aircraft altitude is 10000 m. We also set, G_r=0.8, factoring in some loss due to the reflection of RFI

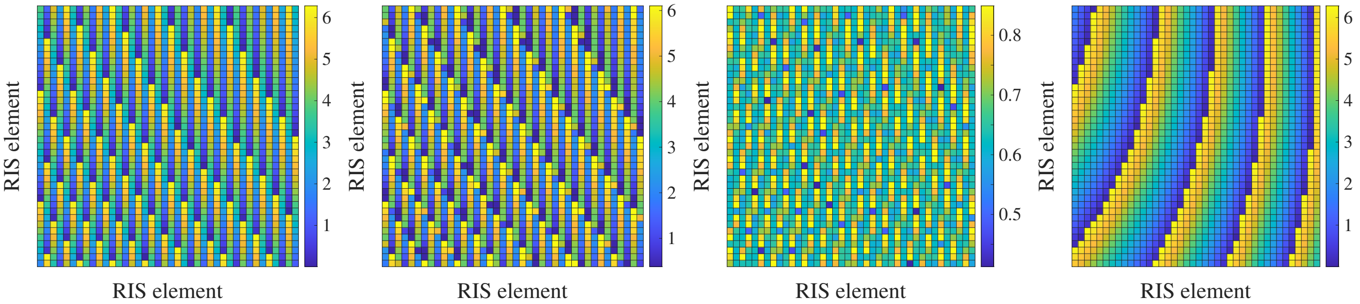

(a) *Phase-*Γ_T*, DoA:*$(-45°, 50°)$ (b) *Phase-*Γ_A (c) *Mag-*Γ_A (d) *Phase-*Γ_T*, DoA:*$(35°, 50°)$

Fig. 3: Target reflection coefficient (Γ_T*) and achieved reflection coefficient (*Γ_A*). Also* Γ_T *varies with the DoA*

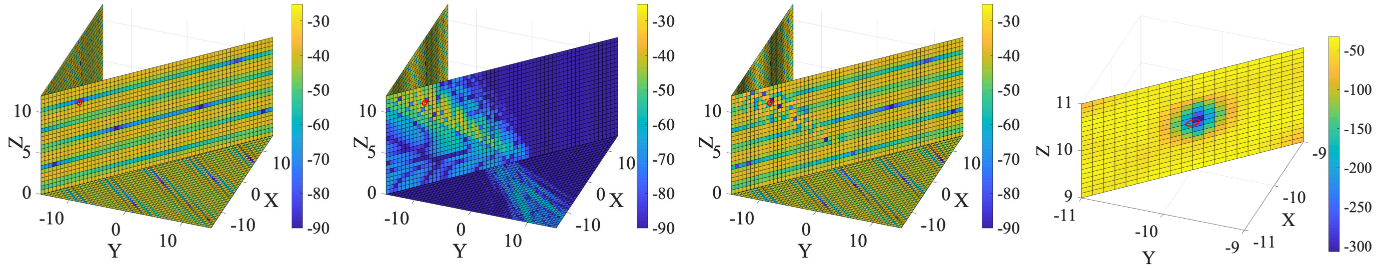

(a) Energy field of the direct RFI from T_x *around the Telescope* *(b) Energy field of the RIS reflected wave towards the* R_x *(c) EM Quiet Zone: RFI is completely canceled at* R_x *(d) Zoomed in EM Quiet Zone at the* R_x *location*

Fig. 4: EM Quiet Zone represents complete cancellation of RFI at R_x*.* R_x *Location: (-10,-10,10), RIS Location: (0,0,0)*

across the RIS array. The DoA and DoR is initially set at ϕ_1=$-45°$ and θ_1=$50°$, ϕ_2=$225°$ and θ_2=$35°$. The array size $M \times N$ is chosen to be 40×40, yielding a $|\Gamma_T|$=0.6 using (16) for different DoAs. These choices limit the ranges of C_{var} and R_{PIN} within practical values obtained in §IV-C.

B. Target and achieved reflection coefficient

We compare the target reflection coefficient, Γ_T and achieved reflection coefficient, Γ_A to verify the RIS element design and its equivalent circuit. Figure 3a shows the phase of Γ_T, obtained from (19). It is evident that the phase pattern within each column and row exhibit periodicity. Thus, if the designed RIS can achieve this Γ_T for one particular column or row, the entire array can achieve the target phase by setting the bias voltage for each diode from one of the 16 possible values. The magnitude, $|\Gamma_T|=$ 0.6 is constant for all the elements for uniformity across the array. Figures 3b and 3c show the phase and magnitude of Γ_A using the circuit model and with the selected part numbers. We notice that the phase and magnitude of Γ_A have very similar periodicity. For comparison, Figure 3d, shows the phase of Γ_T for a different DoA, which exhibits very different periodicity than Figure 3a.

C. Cancelling RFI from a fixed source

We compare the energy field surrounding the receiver, R_x with and without the RIS-based cancellation to illustrate the impact of the RIS reflected beam, in Figure 4. To clearly visualize the energy field in a 3D space, we show the cross-sectional plane along the RIS and R_x. Figure 4a illustrates the energy field of the direct RFI originating from the T_x at the vicinity of R_x. It results in periodic variations of the energy levels separated by regions of high and low energy, which depend on λ. Figure 4b shows the energy field of the amplitude and phase-adjusted RIS reflected beam. It is interesting to observe from the color bar that *the highest power point of the reflected beam need not coincide with the exact location of the* R_x. This indicates that the RIS array is not specifically designed to direct and focus all the energy at R_x. The overlap of the EM fields of the direct and the reflected RFI creates an *EM Quiet Zone* at R_x, as shown in Figure 4c. The dark blue area surrounding the telescope signifies a region with very low energy levels through the use of the RIS compared to figure 4a. A closer view of the EM Quiet Zone in Figure 4d confirms the existence of the EM Quiet Zone at R_x, confirming the cancellation.

To express partial cancellation, we define residual RFI as,

$$\zeta = a_d e^{j\phi_d} + \sum_{m=1}^{M} \sum_{n=1}^{N} a_{m,n} \Gamma_{m,n} e^{j\phi_{m,n}} \tag{33}$$

ζ represents the combined gain and phase shift resulting from the superposition of the energy fields of the direct and the reflected waves. A non-zero value of ζ is a measure of the residual RFI at the telescope.

Therefore, the relative cancellation error is,

$$\zeta_r = \left|\zeta / a_d e^{j\phi_d}\right|^2 \tag{34}$$

For a fixed source and other simulation parameters mentioned above, the relative residual error, ζ_r=1.0181×10^{-4}, which is

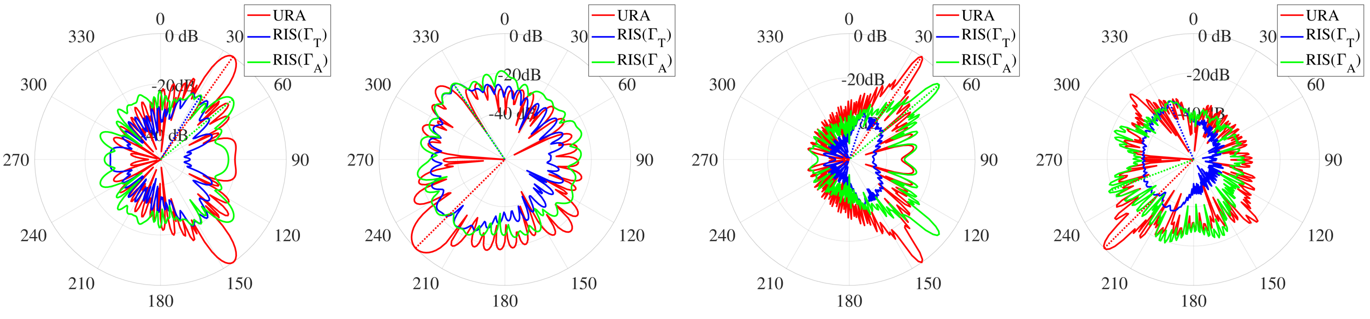

(a) Az cut, θ_2 = 35° *(b) El cut, ϕ_2 = 225°* *(c) Az cut, θ_2 = 35°* *(d) El cut, ϕ_2 = 225°*

Fig. 5: Comparing beam patterns between using URA and RIS array. (a,b): $40{\times}40$ *and (c,d):* $100{\times}100$

a very encouraging result.

D. Comparing with URA Beamforming

We compare the radiation pattern of the RIS and that generated by an Uniform Rectangular Array (URA) of the same size, as shown in figure 5. The red-colored beam pattern illustrates the URA beam directed straight towards the telescope. Meanwhile, the blue-colored pattern represents the RIS reflected beam with the target reflection coefficient Γ_T, and the green-colored pattern shows the reflected beam with the achieved reflection coefficient Γ_A. Figures 5a and 5b shows the azimuth (Az) and elevation (El) cut of the beam patterns obtained with an RIS and URA size of $40{\times}40$ respectively. Similarly, figures 5c and 5d shows the patterns with a RIS and URA size of $100{\times}100$. From figures 5a and 5b, it is apparent that the URA beam is precisely aligned towards the telescope's position so that the peak of the main lobe coincide with the DoR, $\phi{=}35°$ and $\theta{=}225°$. However, the main lobe of the RIS beam need not align precisely with the telescope's position. This also supports the observations in Figure 4d. Therefore, it is not a requirement for the main lobe to be precisely centered at R_x. Figures 5c and 5d further emphasize this point even for narrower beamwidth for larger arrays.

E. Canceling RFI from mobile source

In this section, we expand the investigation from single DoA to multiple DoAs, which is common for a mobile RFI source like and aircraft. However, from a practical stand-point, RFI cancellation either becomes unnecessary or impossible in the following situations: (i) If the elevation, θ of T_x very small, indicating the source is at or near the horizon and direct RFI is very small, rendering cancellation as unnecessary; and (ii) As $\theta{\to}90°$, the T_x is very close to the telescope and cancellation becomes very challenging due to elevated RFI levels. In such cases, the telescope needs to fall back on convectional excision techniques or employ other methods of cancellation [17], [18]. Therefore, we define the set of possible DoAs as, $El{\in}\{30°{:}70°\}$ and $Az{\in}\{-180°{:}180°\}$.

The values of M, N, G_r are fixed once the RIS is deployed along with λ. From (16) we know that $|\Gamma|$ only depends on the ratio of r_1 and d. If we consider $r_1{\approx}d$ for a distant T_x, it yields a relatively constant $|\Gamma_T|{\approx}0.6$. Based on variations of DoA, $|\Gamma_T|$ may slightly exceed or fall short of this constant value.

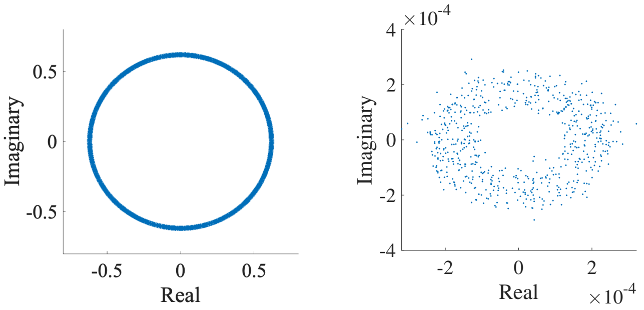

(a) Target reflection coefficient *(b) Cancellation error*

Fig. 6: Cancellation error for different DoA

Therefore, the complex Γ_T for all elements for different DoAs resembles a ring-like pattern with a narrow range of $|\Gamma_T|$ but a range of $\angle\Gamma_T{\in}\{0{:}2\pi\}$ as shown in Figure 6a. Figure 6b shows the corresponding ζ_r for each DoA. The results show that our RFI cancellation system consistently achieves small values of ζ_r across multiple DOAs.

VI. RELATED WORK

Recent literature on RIS have propelled significant advances in wireless communication. The field of research surrounding the application of RIS and diverse design methods is quite vast [19]–[21]. In [22], the authors utilize the integrate phase-shift and radiation pattern using PIN diodes and improved beamforming efficiency without relying on traditional phase shifters. [23] introduce a prototype RIS-aided wireless communication system, with innovative control of reflection coefficients through adjusting patch impedance for beamforming. This study pioneers an adaptive reflection coefficient algorithm based on feedback, ensuring intelligent reflection without modifying existing communication standards. [1] focuses on directional reflection, implementing 2430 unit cells with varactor diodes for precise phase regulation. This directional control aligns with [24], positioning RIS as a promising technology for extending wireless coverage through a switch-per-cell design, emphasizing low power consumption and high SNR gain.

In [25], the authors explore RIS with continuous phase shift tuning, for ambient backscatter communication. This is achieved through dynamic control of phase of individual unit cells using varactor diodes. In [26], an analytical model emphasizing the role of varactor diode is proposed for controlling the reflection coefficient for beamforming. While [27] propose a design with metallic vias ensuring insensitivity to incident EM wave angles, enhancing the stability of RIS. Meanwhile, the authors in [28] introduces a programmable element with separate control over amplitude and phase, utilizing to construct RIS arrays generating scattered beams with adjustable characteristics. However, the shared transmission line for both PIN and varactor restrict the freedom to control the reflection amplitude and phase. None of these design has the ability to independently control the magnitude and phase of reflection coefficient, which is one of the strengths of this work. A major distinction of the proposed approach from the literature is the fact that our design is specifically geared to cancel any signal, such as RFI instead of conventional beamforming in a specific direction. To realize this in practice, we introduce two independent bias circuits for the PIN and varactor diodes to allow simultaneous control of amplitude and phase to achieve a variety of target reflection coefficient with very small error.

VII. CONCLUSION

In this work, we propose a novel RIS design for signal cancellation in 3-dimensions. We developed a blueprint for design and fabrication of a RIS array combine PIN and varactor diode together for independent control over phase and amplitude of the reflection coefficient of each RIS elements. Our simulated experiments for a single DOA as a representative sample exemplify the efficacy of our approach. We show the generality of our design for a range of DoA, which is critical for continuous cancellation of RFI from airborne sources. We believe that successful prototyping of the RIS array will improve the sensitivity of Radio Telescopes in ways that is not currently possible, ensuring the integrity of RAS while promoting spectrum sharing among various types of users.

ACKNOWLEDGEMENT

This work is funded by the National Science Foundation SWIFT Program (Award Number - 2229496).

REFERENCES

[1] A. Araghi, M. Khalily, M. Safaei, A. Bagheri, V. Singh, F. Wang, and R. Tafazolli, "Reconfigurable intelligent surface (ris) in the sub-6 ghz band: Design, implementation, and real-world demonstration," *IEEE Access*, vol. 10, pp. 2646–2655, 2022.

[2] X. Wei, D. Saha, G. Hellbourg, and A. Dutta, "Multistage 2d doa estimation in low snr," in *ICC 2023-IEEE International Conference on Communications*. IEEE, 2023, pp. 2785–2790.

[3] A. Díaz-Rubio, V. S. Asadchy, A. Elsakka, and S. A. Tretyakov, "From the generalized reflection law to the realization of perfect anomalous reflectors," *Science advances*, vol. 3, no. 8, p. e1602714, 2017.

[4] R. Cohen, "The threat to radio astronomy from radio pollution," *Space Policy*, vol. 5, no. 2, pp. 91–93, 1989.

[5] Z. Zou, X. Wei, D. Saha, A. Dutta, and G. Hellbourg, "Scisrs: Signal cancellation using intelligent surfaces for radio astronomy services," in *GLOBECOM 2022-2022 IEEE Global Communications Conference*. IEEE, 2022, pp. 4238–4243.

[6] R. S. Committee *et al.*, "Minimum aviation system performance standards for automatic dependent surveillance broadcast (ads-b)," Technical report, January, Tech. Rep., 1998.

[7] M. H. Cohen, "The owens valley radio observatory: Early years," *Engineering and Science*, vol. 57, no. 3, pp. 8–23, 1994.

[8] R. Li, B. Guo, M. Tao, Y.-F. Liu, and W. Yu, "Joint design of hybrid beamforming and reflection coefficients in ris-aided mmwave mimo systems," *IEEE Transactions on Communications*, vol. 70, no. 4, pp. 2404–2416, 2022.

[9] J. C. Liang, Q. Cheng, Y. Gao, C. Xiao, S. Gao, L. Zhang, S. Jin, and T. J. Cui, "An angle-insensitive 3-bit reconfigurable intelligent surface," *IEEE Transactions on Antennas and Propagation*, vol. 70, no. 10, pp. 8798–8808, 2021.

[10] Skyworks-Inc, "SMV1405 to SMV1430 Series: Abrupt Junction Tuning Varactors," https://www.skyworksinc.com/-/media/SkyWorks/Documents/Products/101-200/SMV1405_1430_Series_200068W.pdf.

[11] MICROSEMI, "Um4000/um4900 high power pin diodes," https://www.microsemi.com/document-portal/doc_view/11318-um4000-um4900-datasheet-pdf.

[12] C. A. Balanis, *Antenna theory: analysis and design*. John wiley & sons, 2016.

[13] Y. Huang, *Antennas: from theory to practice*. John Wiley & Sons, 2021.

[14] T. C. Edwards and M. B. Steer, *Foundations of interconnect and microstrip design*. Wiley Online Library, 2000.

[15] D. M. Pozar, *Microwave engineering*. John wiley & sons, 2011.

[16] C. R. Paul, *Analysis of multiconductor transmission lines*. John Wiley & Sons, 2007.

[17] M. Careem, S. Chakaraborty, A. Dutta, D. Saha, and G. Hellbourg, "Spectrum sharing via collaborative rfi cancellation for radio astronomy," in *2021 IEEE International Symposium on Dynamic Spectrum Access Networks (DySPAN)*, 2021, pp. 97–104.

[18] S. Chakraborty, D. Saha, A. Dutta, and G. Hellbourg, "Loci: Learning low overhead collaborative interference cancellation for radio astronomy," in *ICC 2023 - IEEE International Conference on Communications*, 2023, pp. 6391–6396.

[19] Y. Liu, X. Liu, X. Mu, T. Hou, J. Xu, M. Di Renzo, and N. Al-Dhahir, "Reconfigurable intelligent surfaces: Principles and opportunities," *IEEE Communications Surveys & Tutorials*, vol. 23, no. 3, pp. 1546–1577, 2021.

[20] Z. Ding, L. Lv, F. Fang, O. A. Dobre, G. K. Karagiannidis, N. Al-Dhahir, R. Schober, and H. V. Poor, "A state-of-the-art survey on reconfigurable intelligent surface-assisted non-orthogonal multiple access networks," *Proceedings of the IEEE*, vol. 110, no. 9, pp. 1358–1379, 2022.

[21] B. Zheng, C. You, W. Mei, and R. Zhang, "A survey on channel estimation and practical passive beamforming design for intelligent reflecting surface aided wireless communications," *IEEE Communications Surveys & Tutorials*, vol. 24, no. 2, pp. 1035–1071, 2022.

[22] L. Dai, B. Wang, M. Wang, X. Yang, J. Tan, S. Bi, S. Xu, F. Yang, Z. Chen, M. D. Renzo, C.-B. Chae, and L. Hanzo, "Reconfigurable intelligent surface-based wireless communications: Antenna design, prototyping, and experimental results," *IEEE Access*, vol. 8, pp. 45 913–45 923, 2020.

[23] X. Pei, H. Yin, L. Tan, L. Cao, Z. Li, K. Wang, K. Zhang, and E. Björnson, "Ris-aided wireless communications: Prototyping, adaptive beamforming, and indoor/outdoor field trials," *IEEE Transactions on Communications*, vol. 69, no. 12, pp. 8627–8640, 2021.

[24] G. C. Trichopoulos, P. Theofanopoulos, B. Kashyap, A. Shekhawat, A. Modi, T. Osman, S. Kumar, A. Sengar, A. Chang, and A. Alkhateeb, "Design and evaluation of reconfigurable intelligent surfaces in real-world environment," *IEEE Open Journal of the Communications Society*, pp. 462–474, 2022.

[25] R. Fara, P. Ratajczak, D.-T. Phan-Huy, A. Ourir, M. Di Renzo, and J. de Rosny, "A prototype of reconfigurable intelligent surface with continuous control of the reflection phase," *IEEE Wireless Communications*, 2022.

[26] F. Costa and M. Borgese, "Electromagnetic model of reflective intelligent surfaces," *IEEE Open Journal of the Communications Society*, vol. 2, pp. 1577–1589, 2021.

[27] J. C. Liang, Q. Cheng, Y. Gao, C. Xiao, S. Gao, L. Zhang, S. Jin, and T. J. Cui, "An angle-insensitive 3-bit reconfigurable intelligent surface," *IEEE Transactions on Antennas and Propagation*, vol. 70, no. 10, pp. 8798–8808, 2022.

[28] J. C. Liang, L. Zhang, Z. W. Cheng, P. Zhang, and T. J. Cui, "Flexible beam manipulations by reconfigurable intelligent surface with independent control of amplitude and phase," *Frontiers in Materials*, vol. 9, 2022.